

NASA Contractor Report 189042  
AIAA-92-0420

1N-34  
51154  
p-13

# Vorticity Dynamics of Inviscid Shear Layers

Jeffrey W. Yokota  
*Sverdrup Technology, Inc.*  
*Lewis Research Center Group*  
*Brook Park, Ohio*

October 1991

Prepared for  
Lewis Research Center  
Under Contract NAS3-25266



National Aeronautics and  
Space Administration

(NASA-CR-189042) VORTICITY DYNAMICS OF  
INVISCID SHEAR LAYERS Final Report  
(Sverdrup Technology) 13 p

CSCL 200

N92-12212

Unclass

G3/34 0051154



# Vorticity Dynamics of Inviscid Shear Layers

Jeffrey W. Yokota  
Sverdrup Technology, Inc.  
NASA Lewis Research Center Group  
Cleveland, Ohio

## Abstract

The inviscid evolution of a two dimensional shear layer is simulated numerically by a scheme based on a kinematic decomposition of the unsteady flow. Lagrangian and Weber transformations of the incompressible Euler equations result in a Clebsch representation that separates the flow field into rotational and irrotational components. These transformations produce the initial construction of the flow field and define its subsequent evolution.

## Introduction

As numerical schemes become more accurate and efficient, computational simulations are being used to investigate flow phenomena of increasing complexity. Analytical methods, while both powerful and informative, are often difficult to apply to nonlinear problems on complex geometries. Numerical techniques, however, allow for the modelling of both geometric and nonlinear complexities. Unfortunately numerical consistency exists only within the limit of infinitesimally small time steps and grid spacings, where the likelihood of having resources large enough to accomplish such calculations remains remote. Thus practical difficulties occur when trying to extract physically meaningful results from simulations of only medium fineness and accuracy. Consequently, one hopes to improve the performance of more moderately accurate schemes (typically second or third order accurate) by incorporating problem-specific flow physics into the numerical solution procedure.

Most currently used inviscid schemes are based on the one dimensional Euler equations and have unquestionably good shock capturing capabilities. Unfortunately their ability to resolve unsteady vortical flows is not yet of equal stature. First, the concept of vorticity does not exist in one dimension and second, correct wave propagation, a major requirement of any unsteady simulation, is not easily satisfied in multidimensions.

Central differenced schemes gather information from all directions and are often the methods of choice for elliptic flow calculations. Their use in hyperbolic calculations, however, requires an explicitly added artificial dissipation which, unless tailored judiciously, can significantly reduce spatial accuracy.

Upwind differenced schemes produce superior one dimensional results since the flow field can be resolved along grid directions coincident with the

physically upwind ones. Unfortunately, extending these concepts to multidimensions is made difficult by the infinite number of directions and waves from which one must choose to upwind. In the present work, the incompressible Euler equations are decomposed into scalar elliptic and hyperbolic equations to take advantage of the benefits of both central and upwind differenced numerical techniques.

Historically, the value of a velocity decomposition scheme could be found in its ability to add rotational effects to steady potential flow calculations.<sup>1,2,3,4</sup> However, the use of velocity decomposition schemes became less common as shock capturing became more refined. With the exception of helicopter wake/rotor interactions,<sup>5,6</sup> where the need to conserve vorticity often outweighs any desire to calculate strong shocks, most inviscid compressible flows are currently simulated with shock capturing schemes. However, despite being restricted to flows with weak shocks, calculations of unsteady vortical flows, such as those associated with fluid mixing, should benefit from a velocity decomposition approach.

An obvious decomposition is the one that splits the flow into rotational and irrotational components.<sup>7,8</sup> Initially this decomposition seems appealing since one hopes to have split the flow into acoustic and vortical fields. Unfortunately, this splitting is not unique since the rotational component can be constructed from the sum of the vortical field and any arbitrary irrotational field (provided this irrotational field is also subtracted from the acoustic component). Thus one cannot assume to have split the flow field into acoustic and vortical components exclusively.<sup>9</sup> The flow equations are, however, decomposed into scalar elliptic and hyperbolic ones, thereby isolating the vortical field within the rotational component which can then be convected by an appropriate upwind scheme.

Thus the hope of this work is to produce a set of kinematically decomposed flow equations, suited for the simulation of unsteady vortical flows, and solved by appropriate central and upwind differenced numerical schemes. To test this approach, a steady shear flow is constructed analytically, reproduced numerically, and then perturbed by an unsteady inflow boundary condition. The inviscid evolution of these inflow disturbances is then simulated from small amplitude wave to nonlinear rollup. The irrotational component of the flow is constructed from the velocity potential solution of a

central differenced continuity equation. This equation is solved by an approximate LU factorization scheme that is written within the framework of the multigrid method. The rotational component of the flow is represented by a series of complex-lamellar fields whose components are convected by an up-wind differenced material derivative. The nonlinear interaction between these components is captured by coupling the rotational and irrotational fields during each time step of the unsteady calculation.

### Analysis

The incompressible Euler equations can be written in the Cartesian coordinate system  $(x, y)$  as

$$\nabla \cdot \vec{v} = 0 \quad (1)$$

$$\frac{Du_i}{Dt} = \frac{\partial u_i}{\partial t} + (\vec{v} \cdot \nabla) u_i = -\frac{1}{\rho} \nabla p \quad (2)$$

where  $\vec{v} = (u, v)$  are the Cartesian velocity components,  $\rho$  is density,  $p$  is pressure, and the material derivative is defined as:

$$\frac{D}{Dt} = \frac{\partial}{\partial t} + (\vec{v} \cdot \nabla) \quad (3)$$

Lagrangian coordinates  $(X, Y)$  satisfy

$$\frac{DX}{Dt} = \frac{DY}{Dt} = 0 \quad (4)$$

where the Cartesian/Lagrangian transformation matrix is defined as:

$$J = \frac{\partial x_i}{\partial X_j} \quad (5)$$

Linear momentum, Eq.(2), is multiplied by the matrix  $J$  to produce the following tensor equation (sum over repeated indices):

$$\frac{D}{Dt} \left( u_i \frac{\partial x_i}{\partial X_j} \right) = \frac{\partial}{\partial X_j} \left( \frac{u_i^2}{2} \right) - \frac{1}{\rho} \frac{\partial p}{\partial X_j} \quad (6)$$

which can then be integrated as follows:

$$\int \frac{D}{Dt} \left( u_i \frac{\partial x_i}{\partial X_j} \right) dt = \int \frac{\partial}{\partial X_j} \left( \frac{u_i^2}{2} - \frac{p}{\rho} \right) dt \quad (7)$$

such that

$$u_i \frac{\partial x_i}{\partial X_j} - a_j(X, Y) = \frac{\partial}{\partial X_j} \int \left( \frac{u_i^2}{2} - \frac{p}{\rho} \right) dt \quad (8)$$

where  $a_j$  is a constant of integration dependant on the material coordinates  $(X, Y)$ . If one defines the Weber transformation:<sup>10,11</sup>

$$\frac{D\phi}{Dt} = \frac{u_i^2}{2} - \frac{p}{\rho} \quad (9)$$

Eq.(8) can then be written:

$$u_i \frac{\partial x_i}{\partial X_j} = A_j + \frac{\partial \phi}{\partial X_j} \quad (10)$$

where  $A_j$  is a constant of integration and

$$\frac{DA_j}{Dt} = 0 \quad (11)$$

Eq.(10) can now be multiplied by the inverse of matrix  $J$  to produce the Clebsch decomposition:

$$u_i = A_j \frac{\partial X_j}{\partial x_i} + \frac{\partial \phi}{\partial x_i} \quad (12)$$

The rotational velocity field at  $t = t_0$  is defined as:

$$u_i^{r0} = \left( u_i - \frac{\partial \phi}{\partial x_i} \right) \Big|_{t=t_0} \quad (13)$$

and if one sets  $X_i = x_i$  at  $t = t_0$ , then  $u_j^{r0} = A_j$  Eqs.(11) and (12) become

$$\frac{Du_j^{r0}}{Dt} = 0 \quad (14)$$

and

$$u_i = u_j^{r0} \frac{\partial X_j}{\partial x_i} + \frac{\partial \phi}{\partial x_i} \quad (15)$$

An unsteady, incompressible, inviscid vortical flow can now be described by the scalar convection equations, Eqs.(4) and (14); continuity, Eq.(1); and the Clebsch decomposition, Eq.(15); provided the initial condition  $X_i = x_i$  is specified at  $t = t_0$ .

### Unsteady Convection Scheme

Convection equations (4) and (14) can be written as the decoupled scalar system:

$$\frac{\partial W}{\partial t} + \frac{\partial F}{\partial x} + \frac{\partial G}{\partial y} = 0 \quad (16)$$

This equation is solved by a cell-centered finite volume scheme that constructs a piecewise linear distribution over each of the finite volumes; characteristically convects information to an intermediate time level; and updates the cell-centered variables with a midpoint rule time integration.

To insure the production of a nonoscillatory solution, at least directionally, the piecewise linear distribution is constructed in a nonoscillatory manner. To avoid excessive amounts of damping, this distribution must be at least uniformly second order accurate. A one-dimensional interpolation can be written:

$$W = W_i + S_i^x(x - x_i) \quad (17)$$

where  $S_i^x$  is the slope over each finite volume. The slope associated with Harten and Osher's uniformly second order accurate UNO2 scheme<sup>12</sup> is written:

$$S_i^x = \frac{\text{Median}(0, W_{i+1/2}^c - W_i, W_i - W_{i-1/2}^c)}{\Delta x/2} \quad (18)$$

where  $W_{i+1/2}^c$  is obtained from a nonoscillatory quadratic interpolation:

$$W_{i+1/2}^c = 0.5(W_i + W_{i+1}) - 0.25D_{i+1/2} \quad (19)$$

where

$$D_{i+1/2} = \minmod(D_i, D_{i+1}) \quad (20)$$

$$D_i = W_{i+1} - 2W_i + W_{i-1}$$

and

$$\begin{aligned} \minmod(a, b) = \\ \text{sign}(a)\max(0, \text{sign}(ab)\min(|a|, |b|)) \end{aligned} \quad (21)$$

Surface data is evaluated at time level  $n + 1/2$  by following characteristics back to their spatial locations at time level  $n$ . For positive convection speeds the surface data at time level  $n + 1/2$  is written:

$$\begin{aligned} W_{i+1/2,j}^{n+1/2} = W_{i,j}^n + S_{i,j}^x \frac{\Delta x}{2} \left(1 - \frac{u_{i+1/2,j}\Delta t}{\Delta x}\right) \\ - S_{i,j}^y \frac{v_{i+1/2,j}\Delta t}{2} \end{aligned} \quad (22)$$

Once the surface data and their fluxes are constructed at the time level  $n + 1/2$ , the cell-centered values are updated by the midpoint rule:

$$\begin{aligned} W_{i,j}^{n+1} = W_{i,j}^n - \Delta t \left( \frac{F_{i+1/2,j}^{n+1/2} - F_{i-1/2,j}^{n+1/2}}{\Delta x} \right. \\ \left. + \frac{G_{i,j+1/2}^{n+1/2} - G_{i,j-1/2}^{n+1/2}}{\Delta y} \right) \end{aligned} \quad (23)$$

where  $F = Wu$  and  $G = Wv$ .

### Steady State Potential Scheme

The continuity equation:

$$\nabla \cdot \vec{v} = \frac{\partial}{\partial x_i} \left( u_j^0 \frac{\partial X_j}{\partial x_i} + \frac{\partial \phi}{\partial x_i} \right) = 0 \quad (24)$$

must be satisfied at each time step and produces the velocity potential  $\phi$ . This equation is solved by the approximately LU factored scheme:

$$\begin{aligned} \left[1 - \mu\alpha(\delta_x^+ + \delta_y^+)\right] \cdot \left[1 + \mu\alpha(\delta_x^- + \delta_y^-)\right] \Delta\phi_{ij} \\ = \alpha\omega(\delta_x u + \delta_y v)_{ij} \end{aligned} \quad (25)$$

where  $\Delta\phi_{ij} = \bar{\phi}_{ij} - \phi_{ij}$ ;  $\mu$  and  $\alpha$  are scalar constants of  $o(1)$ ;  $\omega$  is a relaxation parameter; and  $\delta^+$ ,  $\delta^-$ , and  $\delta$  are forward, backward, and central difference operators. The residual, Eq.(24), is approximated by a finite volume formulation that constructs fluxes on the faces of each mesh cell. The scalar system is then solved by two explicit sweeps through the domain, similar to the procedures developed for two factored implicit time marching schemes.<sup>13,14</sup>

To illustrate the potential convergence properties of this scheme, a von Neumann stability analysis is performed on the one dimensional equation:

$$\frac{\delta^2 \phi}{\delta x^2} = 0 \quad \text{where} \quad \phi_j^n = G^n e^{i\beta x_j}$$

The approximate LU factored scheme

$$\left[1 - \mu\alpha\delta_x^+\right] \cdot \left[1 + \mu\alpha\delta_x^-\right] \Delta\phi_j = \alpha\omega\delta_{xx}\phi_j$$

has the growth factor

$$G = \frac{1 - 4\alpha[\omega - \mu(1 + \mu\alpha)]\sin^2\left(\frac{\beta\Delta x}{2}\right)}{1 + 4\mu\alpha(1 + \mu\alpha)\sin^2\left(\frac{\beta\Delta x}{2}\right)}$$

and is plotted in Fig.1 for  $\mu = 0.5$ ,  $\alpha = 5.3$ , and  $\omega = 1.9$ . The growth factor has a strong high wave number damping that makes this scheme receptive to multigrid acceleration. Thus the approximate LU scheme is written within the framework of the multigrid method to accelerate these calculations to a steady state.

### Analytical Steady Flow

A steady, quasi-two dimensional shear layer can be modelled<sup>15</sup>:

$$u = \bar{u}[1 + R \tanh \beta] \quad (26)$$

$$v = 0 \quad (27)$$

where  $\beta = 0.5(y - y_c)/\theta$ ;  $\bar{u} = 0.5(u_1 + u_2)$ ;  $\Delta u = u_2 - u_1$ ;  $R = 0.5\Delta u/\bar{u}$ ;  $\theta$  is the momentum thickness;

$y_c$  is the centerline; and  $u_1$  and  $u_2$  are the velocities of the two coflowing streams. A Clebsch decomposition that satisfies Eqs.(1), (4), (14), (15), (26), and (27) can be written as:

$$u^{r0} = \bar{u}[1 + R \tanh \beta] - u_1 \quad (28)$$

$$v^{r0} = 0 \quad (29)$$

$$X = x - \bar{u}t[1 + R \tanh \beta] \quad (30)$$

$$Y = y \quad (31)$$

$$\phi = u_1 x + \frac{\bar{u} R t}{2} \tanh \beta [\Delta u + \bar{u} R \tanh \beta] \quad (32)$$

### Numerical Aspects

Shear layer calculations, characterized by  $u_1 = 4.0 \text{ m/s}$ ;  $u_2 = 8.0 \text{ m/s}$ ; and  $\theta = 2.0 \text{ mm}$ , are performed on a  $192 \times 96$  grid (Fig.2). This grid has a uniform streamwise spacing of  $1.6 \text{ mm}$  and is algebraically stretched in the cross-stream direction. The cross-stream distribution has approximately 30 cells within the initial shear layer, 10 of which are within the momentum thickness. The smallest cell is  $0.2 \text{ mm}$  thick and located at the centerline, while the computational domain is approximately  $0.1 \text{ m}$  wide and  $0.3 \text{ m}$  long.

Eq.(30) suggests that an infinite stretching and shearing of the  $X$  material lines is produced as  $t \rightarrow \infty$ . Thus calculations of a long duration are limited in value, since physical viscosity normally acts to dampen this shearing. Furthermore, at the centerline of the shear layer ( $\beta = 0$ ), the gradient  $\frac{\partial X}{\partial y} \rightarrow \infty$  as  $t \rightarrow \infty$  and thus Eq.(27)

$$v = \frac{\partial \phi}{\partial y} + u^{r0} \frac{\partial X}{\partial y} = 0$$

becomes increasingly difficult to satisfy numerically. In essence it becomes numerically indeterminant. Thus cross-stream velocity disturbances, capable of triggering the shear instability, are likely to be generated at the centerline. Despite these limitations, for  $t \ll \infty$ , the short term dynamics of rapidly growing initial disturbances can be simulated by these inviscid equations.

The steady flow is reproduced numerically to evaluate the scheme's fidelity. Even though the flow is steady, the  $X$  material lines' time dependant behavior can be used to evaluate the scheme's performance. The initial conditions are constructed analytically at  $t = 0$  and the velocity potential is recast as a perturbation on a uniform flow. Thus:

$$\phi = u_1 x + \tilde{\phi} \quad (33)$$

An inviscid noflux or parallel flow condition

$$\frac{\partial u^{r0}}{\partial y} = \frac{\partial \tilde{\phi}}{\partial y} + u^{r0} \frac{\partial X}{\partial y} = 0 \quad (34)$$

is specified at both the top and bottom boundaries of the domain while the outflow condition

$$\frac{\partial^2 u^{r0}}{\partial x^2} = \frac{\partial^2 X}{\partial x^2} = \frac{\partial^2 \tilde{\phi}}{\partial y^2} + \frac{\partial}{\partial y} \left( u^{r0} \frac{\partial X}{\partial y} \right) = 0 \quad (35)$$

and:

$$\tilde{\phi}(x_l, y_b) = 0 \quad (36)$$

is specified at  $x = x_l$ . A steady inflow condition

$$\begin{aligned} u^{r0} &= \bar{u} \left[ 1 + R \tanh \beta \right] - u_1 \\ v^{r0} &= \frac{\partial \tilde{\phi}}{\partial x} = 0 \\ \frac{\partial X}{\partial x} &= 1 \end{aligned} \quad (37)$$

is specified at  $x = x_0$ .

Once the scheme's fidelity is verified, the rollup of the shear layer is accelerated by oscillating inflow disturbances. The inflow boundary condition, Eq.(37), is modified with an oscillating centerline:

$$\begin{aligned} \beta &= \frac{(y - \tilde{y}_c)}{2\theta} \\ \tilde{y}_c &= y_c + K\theta \sin(\omega t) \\ \omega &= \frac{2\pi S_n \bar{u}}{\theta} \end{aligned} \quad (38)$$

where  $S_n = 0.032$  is the Strouhal number associated with the shear layer's natural frequency<sup>15</sup> and  $K$  is a scalar constant. The initial rollup of the shear layer results from the inviscid shear flow instability<sup>16</sup> and should be simulated accurately. Subsequent development may not evolve correctly since vortices grow through the continuous ingestion of irrotational fluid, and vortex pairing can occur at saturation.<sup>17</sup> However, a kinematic description assumes a continuous mapping of the material lines which can undergo stretching and folding but not breakage and amalgamation. Consequently, an inviscid simulation of these growing disturbances is most valid during their initial amplification. Despite these limitations, results from a kinematic-based scheme should contribute to the understanding of fluid mixing because

from a kinematical viewpoint fluid mixing is the efficient stretching and folding of material lines and surfaces<sup>18</sup>

Furthermore, the tagging of homogenous subsonic flows, both experimentally and numerically, is often made difficult by the rapid diffusion of the marker

species. Thus coherent structures are often visualized through Schlieren photographs of stratified flows.<sup>19</sup> Consequently, a kinematic-based scheme, capable of quantitative rather than simply qualitative flow visualization, would be valuable.

## Results

The first test case is a numerical reproduction of the analytical steady flow. A constant time step size of 0.01 *ms* is used in this calculation. Since this steady flow simulation is both two dimensional and inviscid, the following collection of first integrals

$$I_n = \int_{\sigma} \omega^n d\sigma \quad n = 1, 2, \dots, \infty \quad (39)$$

where  $\omega$  is vorticity, should remain constant over the computational domain. As a measure of the scheme's ability to reproduce this flow, changes in circulation ( $I_1$ ) and enstrophy ( $I_2$ ), as well as the maximum absolute error in the  $X$  material lines, are monitored. The error in  $X$  is calculated with respect to the analytical solution, Eq.(30); normalized by  $\theta$ ; and meaningful only while the flow remains steady.

To illustrate the convergence acceleration produced by the multigrid scheme, both single and multigrid convergence histories of the potential calculation at  $t = 0.01$  *ms* are shown in Fig.3. A six multigrid level W cycle converged the average residual to  $o(10^{-14})$  in roughly four iterations, each of which is equivalent to approximately 25.7 work units or fine grid calculations.

The initial conditions are assumed to exist for  $-\infty < x < +\infty$  but in Fig.4 are shown only within the domain encompassed by the computational grid. While the calculated flow remains steady, the  $u^{r0}$  material lines remain identical to the initial condition (Fig.4a) and the  $X$  lines, as predicted from the analytical solution, shear continuously with the flow (Fig.5).

This simulation also tests the inflow/outflow boundary conditions since upstream travelling disturbances, orders of magnitude larger than the interior truncation errors of the discretized equations, are often generated from downstream boundary conditions. This problem is acute for zeroth order extrapolations but seems not to exist, at least within the time duration of interest, for a first order treatment. One would expect to see significant variations in circulation and/or exponential growth in enstrophy if the boundary conditions were triggering the shear flow instability. In fact, both circulation (Fig.6) and enstrophy (Fig.7) remained essentially constant with only an extremely small error in the  $X$  material field (Fig.8) evident during the first 6000 time steps ( $t < 60$  *ms*). Although this error grows as it is convected, its growth is not exponential and will not reach a size large enough to render the flow unsteady for some time.

In fact, it is only after these first 6000 time steps that one begins to see the excitation of the shear flow instability and the start of its exponential growth. Cross-stream gradients of the  $X$  material field increase in magnitude; with this behavior comes an increasing potential to generate centerline disturbances. Any existing initial disturbances do not grow exponential from  $t = 0$  and thus the shear instability is more likely to have been triggered by centerline disturbances generated at  $t > 50$  *ms*. To observe the rollup of the shear layer within a more timely fashion and without the question of its numerical origin, one must add some physical forcing to the flow. By forcing the flow, the rollups can be generated before the material lines have sheared beyond a questionable accuracy.

The second test case is the streamwise development of a forced shear layer. The amplitude of the centerline oscillation is one tenth the momentum thickness and therefore confined to within the width of the smallest mesh cell. The frequency of this oscillation corresponds to the natural frequency Strouhal number of  $S_n = 0.032$  and a constant time step size of 0.01 *ms* is again used in the time advancement. This inviscid simulation is most valid in regions where the forced disturbances are being amplified and the resulting vortices are becoming fully developed. Conversely, the accuracy of an inviscid approach is likely to be reduced within preceding regions where the vortices can pair and amalgamate.

Within the shear layer, the discrete contours of the  $u^{r0}$  material lines are equivalent to streaklines passing through the inflow boundary. The evolution of these material lines is an important aspect of flow visualization since streaklines can often reveal more information about an unsteady flow than either streamlines or pathlines.<sup>20</sup>

The evolution of the  $u^{r0}$  and  $X$  material lines is shown in Fig.9 and Fig.10 where one can see the shear flow instability develop from small amplitude wave to nonlinear rollup. The linear growth of these small amplitude waves can be seen in both the  $u^{r0}$  (Fig.9a-b) and the  $X$  (Fig.10a-b) material fields. A distinct steepening of the  $u^{r0}$  material lines can be observed in Fig.9b with their eventual rollup occurring with subsequent evolution. The leading vortex quickly becomes saturated (Fig.9d) while subsequent vortices continue to grow as they convect downstream. Since this is an inviscid simulation, the internal rollups of the material lines are somewhat removed from the more smoothly evolving viscous phenomena. The inviscid shearing of the  $X$  material lines produces a temporally increasing cross-stream gradient that, when disturbed, can rollup infinitely. A simple spiraling, however, does not occur because within these vortical rollups, the material lines are becoming increasingly difficult to resolve. From a numerical perspective, the material lines are not just passively convected by the flow but rather coupled

to its construction. Moreover, the accuracy of the computed flow field is related directly to the resolution of the material fields. Again it is the gross shapes of the initial rollups that are most accurately captured inviscidly. Subsequent rollups are not produced by the initial instability; are often the result of vortex pairing; and the accuracy of their simulation is more likely to be dominated by viscosity, or the lack thereof.

The evolution of an individual  $X$  material line is shown in Fig.11. This line originates outside of the domain and is convected through the inflow boundary condition. The flow is assumed to be steady upstream of the boundary and relative to the oscillating centerline. Within Fig.11 one can see the material line stretch and fold as it convects downstream through the large vortical structures. Within the time duration shown from Fig.11a to Fig.11e, the length of this material line has increased approximately 48 percent. By comparing these results to the simulation of the analytical steady flow, one can attribute 26 percent of this stretching to the presence of the vortical rollups.

Oscillations generated by the inflow forcing can be seen in the circulation history, Fig.12. The magnitude of these growing oscillations is within 0.18 percent and are likely to be overdamped by schemes whose numerical stability depends upon explicitly added artificial dissipation. The enstrophy history consists of an initially linear growth that transitions into an exponential one after approximately 30  $ms$ , or three cycles of the inflow forcing (Fig.13). This transition corresponds to the steepening of the small amplitude waves which can be seen in Figs.9c-d. Flow disturbances grow exponentially from  $t = 0$  and are reflected in the error history of the  $X$  material field, Fig.14. This error grows exponentially from  $t = 0$  and ceases to be meaningful once the shear instability becomes nonlinear. Comparisons to the analytical steady flow are limited once the flow becomes fully unsteady.

The stretching and redistribution of the shear layer are depicted in the evolution of the  $X$  material field's cross-stream gradients, Fig.15. For visual clarity only the largest 10 percent of the gradient field is contoured within each of these figures. One can see how the shear layer bends, breaks (Fig.15c), and ultimately evolves into a number of discrete structures. Once the initial breakage occurs, the shear layer continues to be drawn, pinched, and redistributed into discrete clumps (Figs.15c-15e). Initially these structures are formed at approximately 10  $ms$  intervals, which corresponds to the period of the inflow forcing. Eventually these structures are stretched and bent into self-similar shapes as they are convected downstream past the vortical rollups (Figs.15f-15j).

## Concluding Remarks

A kinematic decomposition of the incompressible Euler equations was derived for the calculation of unsteady vortical flows. Towards this goal, both a uniformly second-order accurate, nonoscillatory convection scheme; and an approximately LU factored multigrid scheme were developed for unsteady and steady calculations, respectively.

To test this approach, and verify the scheme's fidelity, a two dimensional steady shear layer was calculated and compared to its analytical solution. An oscillating inflow was then introduced to accelerate the shear layer's rollup. The bending and stretching of the material lines as they are convected past the growing vortical disturbances could be seen in these simulations.

The value of this kinematic-based scheme can be found within the quantitative visualization of fluid mixing. Rapidly evolving phenomena can be simulated inviscidly, while calculations of long duration or of time periodic flows will require the inclusion of physical viscosity.

## Acknowledgments

It is with pleasure that I acknowledge a number of helpful conversations with Dr. John Adamczyk of NASA Lewis and Drs. Kristine Dugas, Edmane Envira, and Ambady Suresh of Sverdrup Technology.

This work was supported by the NASA Lewis Research Center under contract NAS3-25266 with Dr. John Adamczyk as monitor.

## References

- [1] Murman, E.M., and Stremel, P.M., "A Vortex Wake Capturing Method for Potential Flow Calculations," AIAA Paper 82-0947, June 1982.
- [2] Lacor, C., and Hirsch, Ch., "Rotational flow calculations in three-dimensional blade passages," ASME Paper 82-GT-316, 1982.
- [3] Grossman, B., "The Computation of Inviscid Rotational Gasdynamic Flows using an Alternate Velocity Decomposition," AIAA Paper 83-1900, Proceedings of the AIAA 6th Computational Fluid Dynamics Conference, Danvers, Massachusetts, July 1983.
- [4] Ecer, A., and Akay, H.U., "A Finite Element Formulation for Steady Transonic Euler Equations," AIAA Journal, vol. 21, no. 3, pp. 343-350, March 1983.
- [5] Steinhoff, J., and Suryanarayana, K., "The Treatment of Vortex Sheets in Compressible Potential Flow," AIAA Paper 83-1881, Proceedings of the AIAA 6th Computational Fluid Dynamics Conference, Danvers, Massachusetts, July 1983.

- [6] Ramachandran, K., Tung, C., and Caradonna, F.X., "The Free-Wake Prediction of Rotor Hover Performance using a Vortex Embedding Method," AIAA Paper 89-0638, AIAA 27th Aerospace Sciences Meeting, Reno, Nevada, January 1989.
- [7] Hawthorne, W.R., "On the Theory of Shear Flows," MIT Gas Turbine Laboratory Report no. 88, October 1966.
- [8] Chang, S.-C., and Adamczyk, J.J., "A New Approach for Solving the Three-Dimensional Steady Euler Equations. I. General Theory," *Journal of Computational Physics*, vol. 60, pp. 23-40, 1979.
- [9] Kraichnan, R.H., "The Scattering of Sound in a Turbulent Medium," *Journal of the Acoustical Society of America*, vol. 25, no. 6, pp. 1097-1104, November 1953.
- [10] Serrin, J., "Mathematical Principles of Classical Fluid Mechanics," *Encyclopedia of Physics*, ed. S. Flugge, Springer Verlag, Berlin, vol. VIII/1, pp. 125-263, 1959.
- [11] Trusdell, C., *The Kinematics of Vorticity*, Indiana University Press, Bloomington, Indiana, 1954.
- [12] Harten, A., and Osher, S., "Uniformly Higher-Order Accurate Nonoscillatory Schemes I," *SIAM Journal of Numerical Analysis*, vol. 24, pp. 279-309, 1987.
- [13] Anderson, W.K., Thomas, J.L., and Whitfield, D.L., "Multigrid Acceleration of the Flux Split Euler Equations," AIAA Paper 86-274, AIAA 24th Aerospace Sciences Meeting, Reno, Nevada, January 1986.
- [14] Yokota, J.W., and Caughey, D.A., "An LU Implicit Multigrid Algorithm for the Three-Dimensional Euler Equations," *AIAA Journal*, vol. 26, pp. 1061-1069, September 1988.
- [15] Ho, C.-M., and Huerre, P., "Perturbed Free Shear Layers," *Annual Review of Fluid Dynamics*, vol. 16, pp. 365-424, 1984.
- [16] Saffman, P.C., "Coherent Structures in Turbulent Flow," in *The Role of Coherent Structures in Modelling Turbulence and Mixing*, Jimenez, J., ed., Lecture Notes in Physics, no. 136, pp. 1-9, 1981.
- [17] Winant, C.D., and Browand, F.K., "Vortex pairing: the mechanism of turbulent mixing-layer growth at moderate Reynolds number," *Journal of Fluid Mechanics*, no. 63, pp. 237-255, 1974.
- [18] Ottino, J.M., *The Kinematics of mixing: stretching, chaos, and transport*, Cambridge University Press, New York, New York, 1990.
- [19] Brown, G.L., and Roshko, A., "On the density effects in turbulent mixing layers," *Journal of Fluid Mechanics*, no. 64, pp. 775-816, 1974.
- [20] Hamma, F.R., "Streaklines in a Perturbed

Shear Flow," *Physics of Fluids*, no. 5, pp. 644-650, 1962.

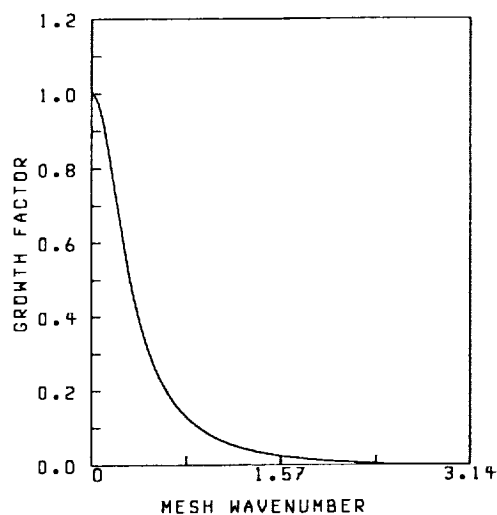
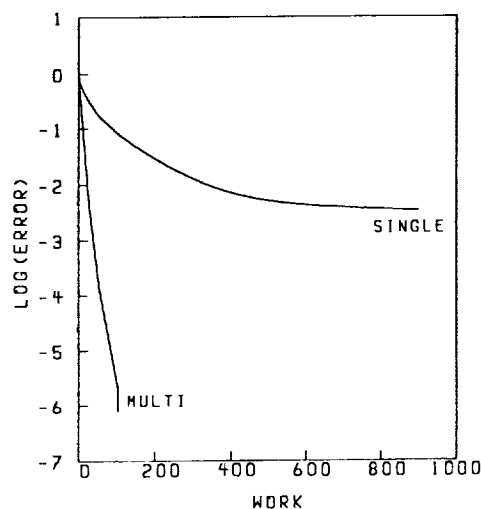


FIGURE 1. - GROWTH FACTOR OF THE LU SCHEME.

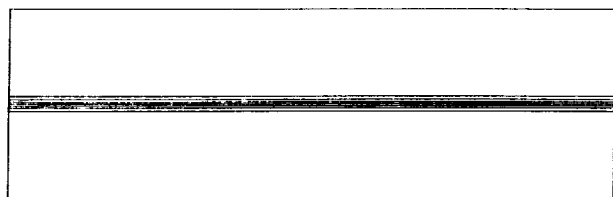


FIGURE 2. - 192x96 GRID.

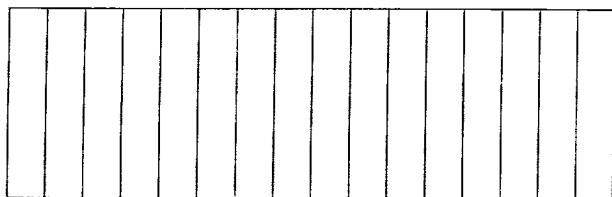


MULTI GRID		SINGLE GRID	
RES1	0.118E-06	RES1	0.515E-06
RES2	0.926E-13	RES2	0.175E-08

FIGURE 3. - CONVERGENCE HISTORY OF THE LU SCHEME AT  $t = 0.01$  MS.

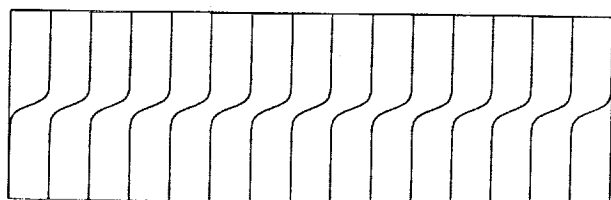


MIN= 0.5000 MAX= 3.5000 INC= 0.5000  
(a)  $u^0$  MATERIAL FIELD.

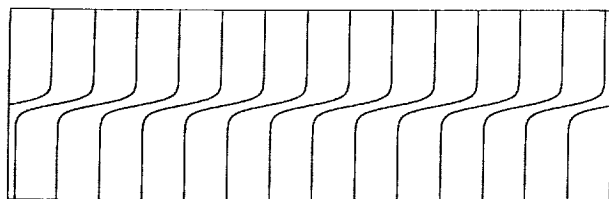


MIN= -0.9992 MAX= -0.6904 INC= 0.0193  
(b) X MATERIAL FIELD.

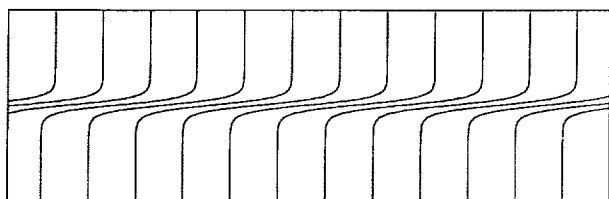
FIGURE 4. - INITIAL CONDITIONS.



MIN= -1.0392 MAX= -0.7104 INC= 0.0205  
(a)  $t = 5.0$  ms.

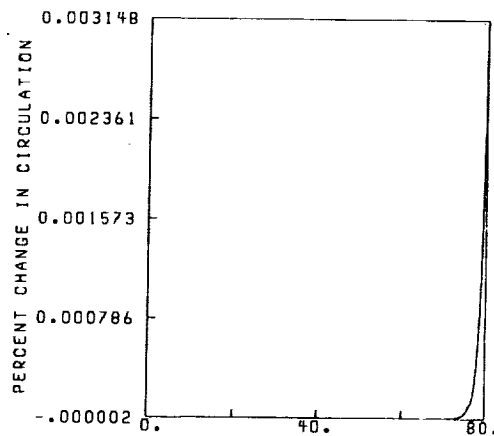


MIN= -1.0792 MAX= -0.7304 INC= 0.0218  
(b)  $t = 10.0$  ms.



MIN= -1.1592 MAX= -0.7704 INC= 0.0243  
(c)  $t = 20.0$  ms.

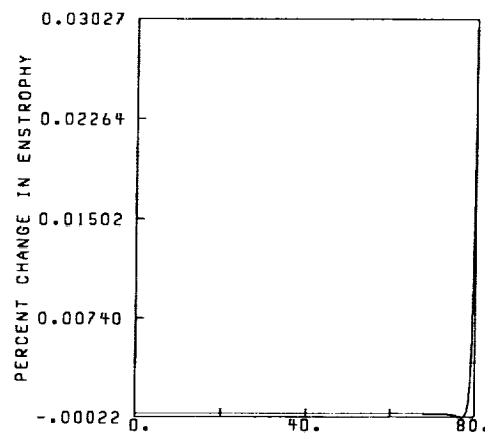
FIGURE 5. - X MATERIAL FIELD: STEADY SHEAR LAYER.



TIME (MILLISECONDS)

INITIAL CIRCULATION = -0.1229E 01

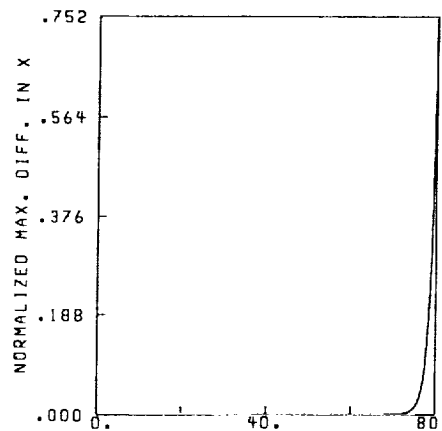
FIGURE 6. - CIRCULATION HISTORY: STEADY SHEAR LAYER.



TIME (MILLISECONDS)

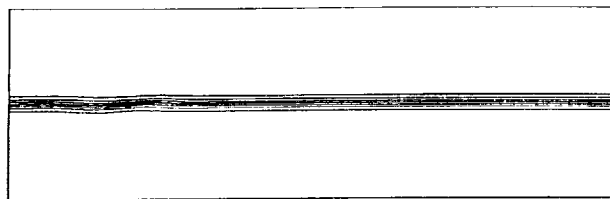
INITIAL ENSTROPY = 0.4093E 03

FIGURE 7. - ENSTROPY HISTORY: STEADY SHEAR LAYER.

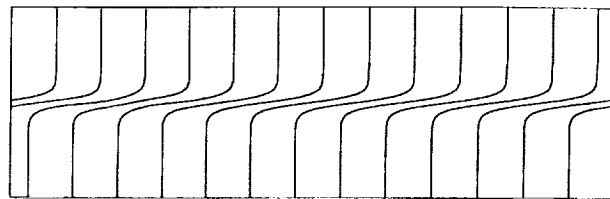


TIME (MILLISECONDS)

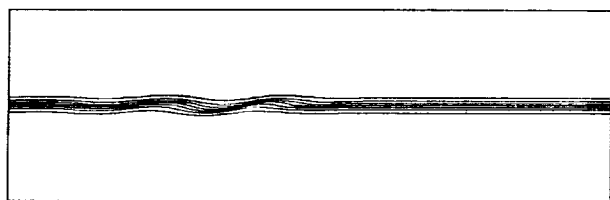
FIGURE 8. - ERROR HISTORY OF THE X MATERIAL FIELD: STEADY SHEAR LAYER.



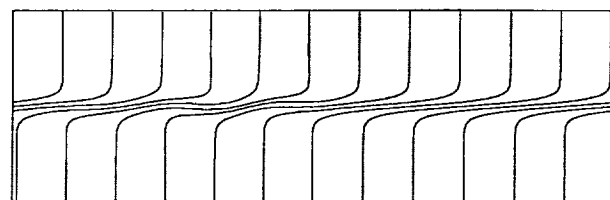
(a)  $t = 15.0$  MS.



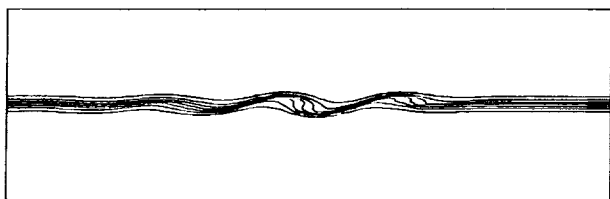
(a)  $t = 15.0$  MS.



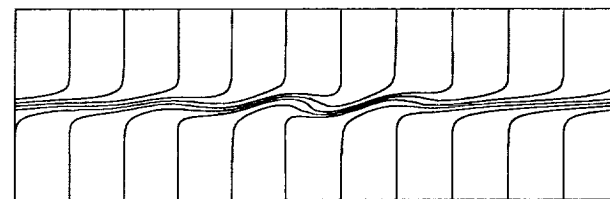
(b)  $t = 25.0$  MS.



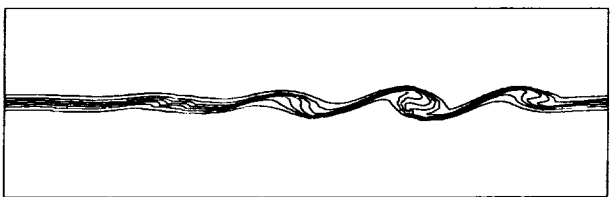
(b)  $t = 25.0$  MS.



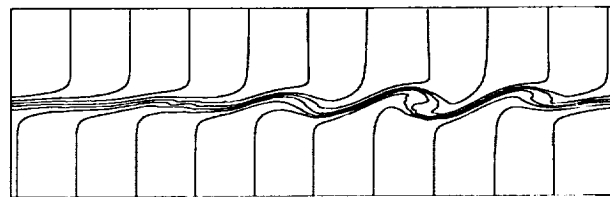
(c)  $t = 35.0$  MS.



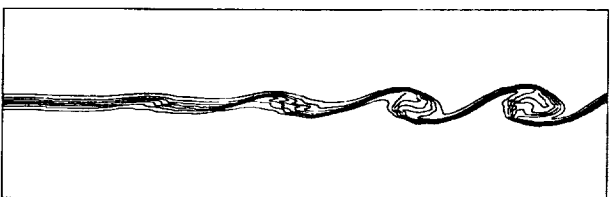
(c)  $t = 35.0$  MS.



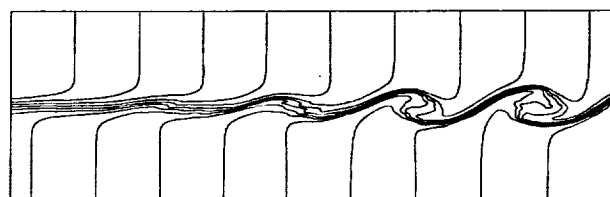
(d)  $t = 45.0$  MS.



(d)  $t = 45.0$  MS.



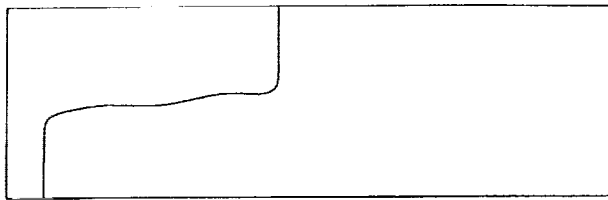
(e)  $t = 55.0$  MS.



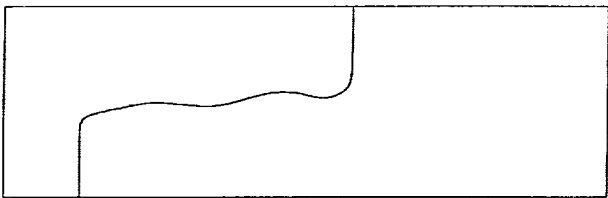
(e)  $t = 55.0$  MS.

FIGURE 9. -  $u^0$  MATERIAL FIELD: FORCED SHEAR LAYER.

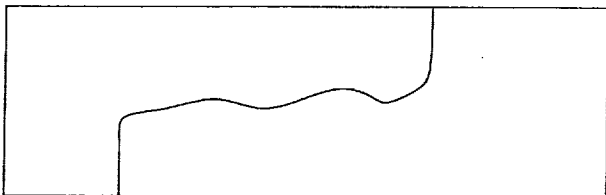
FIGURE 10. -  $X$  MATERIAL FIELD: FORCED SHEAR LAYER.



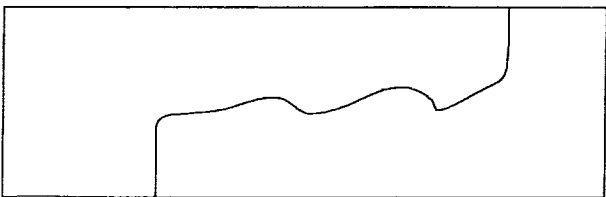
(a)  $t = 30.0$  ms.



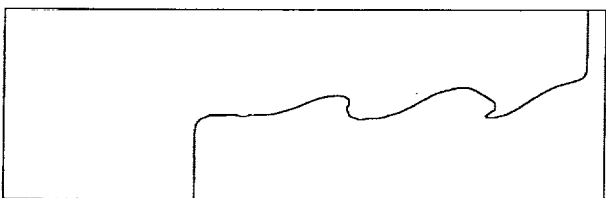
(b)  $t = 35.0$  ms.



(c)  $t = 40.0$  ms.

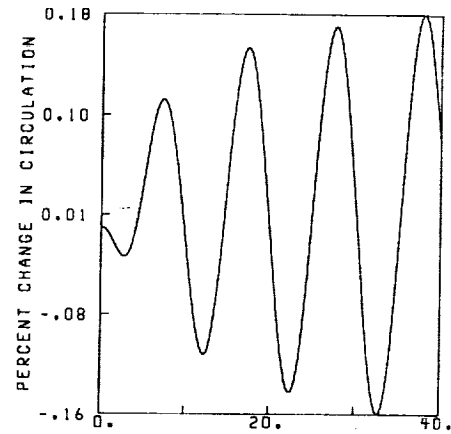


(d)  $t = 45.0$  ms.



(e)  $t = 50.0$  ms.

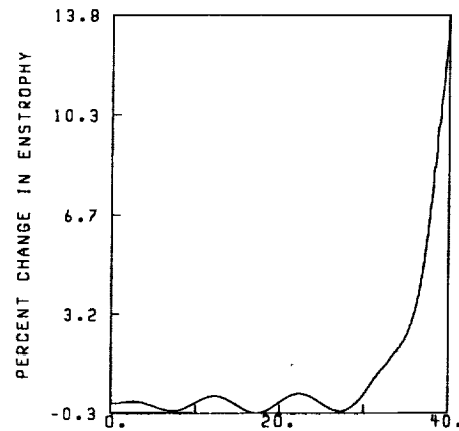
FIGURE 11. -  $X = -1.10$  MATERIAL LINE: FORCED SHEAR LAYER.



TIME (MILLISECONDS)

INITIAL CIRCULATION =  $-0.1229E 01$

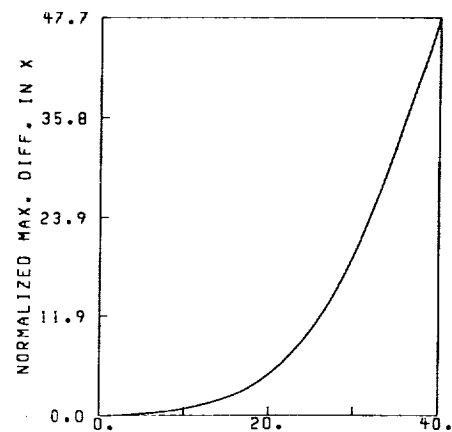
FIGURE 12. - CIRCULATION HISTORY: FORCED SHEAR LAYER.



TIME (MILLISECONDS)

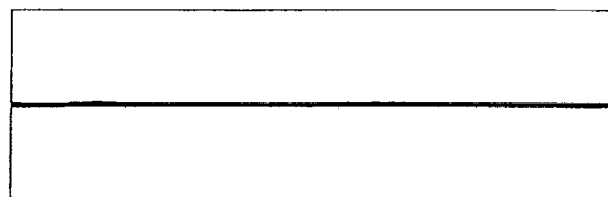
INITIAL ENSTROPY =  $0.4093E 03$

FIGURE 13. - ENSTROPY HISTORY: FORCED SHEAR LAYER.

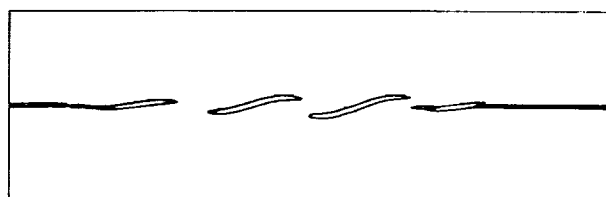


TIME (MILLISECONDS)

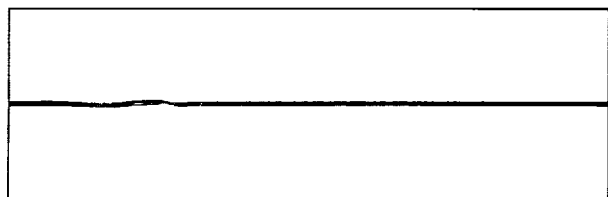
FIGURE 14. - ERROR HISTORY OF THE  $X$  MATERIAL FIELD: FORCED SHEAR LAYER.



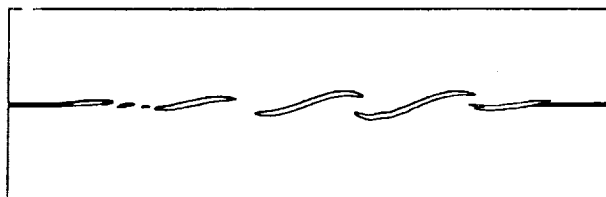
$\text{MIN} = -0.505\text{E } 01$   $\text{MAX} = 0.000$   
(a)  $t = 10.0$  MS.



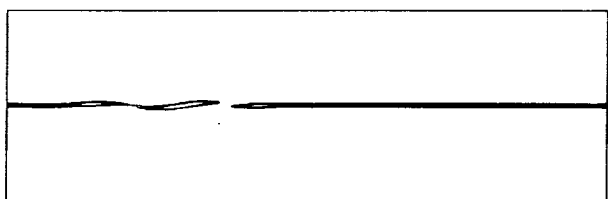
$\text{MIN} = -0.179\text{E } 02$   $\text{MAX} = 0.000$   
(f)  $t = 35.0$  MS.



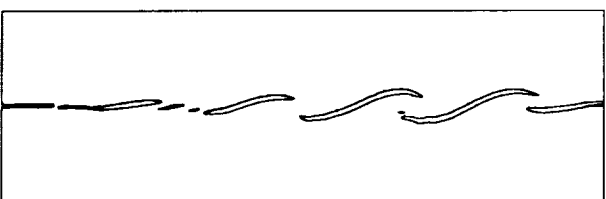
$\text{MIN} = -0.764\text{E } 01$   $\text{MAX} = 0.000$   
(b)  $t = 15.0$  MS.



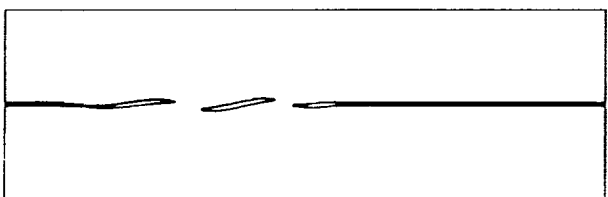
$\text{MIN} = -0.204\text{E } 02$   $\text{MAX} = 0.000$   
(g)  $t = 40.0$  MS.



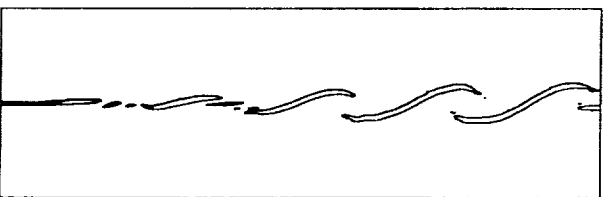
$\text{MIN} = -0.102\text{E } 02$   $\text{MAX} = 0.000$   
(c)  $t = 20.0$  MS.



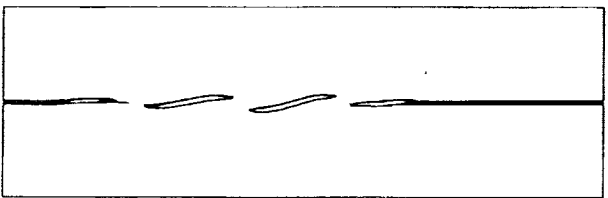
$\text{MIN} = -0.231\text{E } 02$   $\text{MAX} = 0.000$   
(h)  $t = 45.0$  MS.



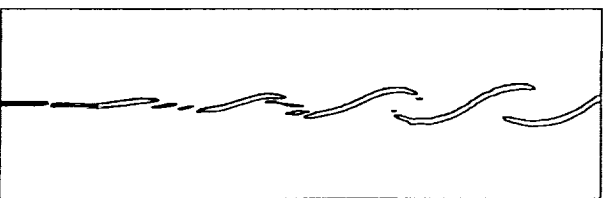
$\text{MIN} = -0.128\text{E } 02$   $\text{MAX} = 0.000$   
(d)  $t = 25.0$  MS.



$\text{MIN} = -0.255\text{E } 02$   $\text{MAX} = 0.000$   
(i)  $t = 50.0$  MS.



$\text{MIN} = -0.153\text{E } 02$   $\text{MAX} = 0.000$   
(e)  $t = 30.0$  MS.



$\text{MIN} = -0.282\text{E } 02$   $\text{MAX} = 0.000$   
(j)  $t = 55.0$  MS.

FIGURE 15. - CROSS-STREAM GRADIENT OF THE X MATERIAL FIELD: FORCED SHEAR LAYER.

REPORT DOCUMENTATION PAGE			Form Approved OMB No. 0704-0188	
Public reporting burden for this collection of information is estimated to average 1 hour per response, including the time for reviewing instructions, searching existing data sources, gathering and maintaining the data needed, and completing and reviewing the collection of information. Send comments regarding this burden estimate or any other aspect of this collection of information, including suggestions for reducing this burden, to Washington Headquarters Services, Directorate for Information Operations and Reports, 1215 Jefferson Davis Highway, Suite 1204, Arlington, VA 22202-4302, and to the Office of Management and Budget, Paperwork Reduction Project (0704-0188), Washington, DC 20503.				
1. AGENCY USE ONLY (Leave blank)		2. REPORT DATE October 1991		3. REPORT TYPE AND DATES COVERED Final Contractor Report
4. TITLE AND SUBTITLE Vorticity Dynamics of Inviscid Shear Layers			5. FUNDING NUMBERS  WU-505-62-52 C-NAS3-25266	
6. AUTHOR(S) Jeffrey W. Yokota				
7. PERFORMING ORGANIZATION NAME(S) AND ADDRESS(ES) Sverdrup Technology, Inc. Lewis Research Center Group 2001 Aerospace Parkway Brook Park, Ohio 44142			8. PERFORMING ORGANIZATION REPORT NUMBER  E-6621	
9. SPONSORING/MONITORING AGENCY NAMES(S) AND ADDRESS(ES)  National Aeronautics and Space Administration Lewis Research Center Cleveland, Ohio 44135-3191			10. SPONSORING/MONITORING AGENCY REPORT NUMBER  NASA CR-189042 AIAA-91-0420	
11. SUPPLEMENTARY NOTES Project Manager, John J. Adamczyk, Lewis Research Academy, NASA Lewis Research Center, (216) 433-5829. Prepared for the 30th Aerospace Sciences Meeting sponsored by the American Institute of Aeronautics and Astronautics, Reno, Nevada, January 6-9, 1992.				
12a. DISTRIBUTION/AVAILABILITY STATEMENT  Unclassified - Unlimited Subject Category 34			12b. DISTRIBUTION CODE	
13. ABSTRACT (Maximum 200 words)  The inviscid evolution of a two dimensional shear layer is simulated numerically by a scheme based on a kinematic decomposition of the unsteady flow. Lagrangian and Weber transformations of the incompressible Euler equations result in a Clebsch representation that separates the flow field into rotational and irrotational components. These transformations produce the initial construction of the flow field and define its subsequent evolution.				
14. SUBJECT TERMS Inviscid flow; Shear layers; Vortex sheets			15. NUMBER OF PAGES 12	
			16. PRICE CODE A03	
17. SECURITY CLASSIFICATION OF REPORT Unclassified	18. SECURITY CLASSIFICATION OF THIS PAGE Unclassified	19. SECURITY CLASSIFICATION OF ABSTRACT Unclassified	20. LIMITATION OF ABSTRACT	